Available online at www.sciencedirect.com
ScienceDirect
Micron 39 (2008) 676–684
micron
www.elsevier.com/locate/micron

Image simulation for electron energy loss spectroscopy

M.P. Oxley *, S.J. Pennycook

Materials Science and Technology Division, Oak Ridge National Laboratory, P.O. Box 2008, Oak Ridge, TN 37831, USA

Abstract

Aberration correction of the probe forming optics of the scanning transmission electron microscope has allowed the probe-forming aperture to be increased in size, resulting in probes of the order of 1 Å in diameter. The next generation of correctors promise even smaller probes. Improved spectrometer optics also offers the possibility of larger electron energy loss spectrometry detectors. The localization of images based on core-loss electron energy loss spectroscopy is examined as function of both probe-forming aperture and detector size. The effective ionization is nonlocal in nature, and two common local approximations are compared to full nonlocal calculations. The affect of the channelling of the electron probe within the sample is also discussed.
Published by Elsevier B.V.

Keywords: EELS; STEM; Localization; Nonlocality

1. Introduction

Electron energy loss spectroscopy (EELS) is a valuable tool in materials science, providing both elemental mapping and local bonding information via near edge structure. The delocalization of the EELS interaction potential has been broadly discussed, see for example Egerton's book and references therein (Egerton, 1996). Many descriptions of the delocalization of the EELS interaction use a single interaction width, such as a classical impact parameter. The effective core-loss ionization interaction is however nonlocal in nature and not easily described in terms of a single variable (Allen and Josefsson, 1995). This is particularly the case for diffracting samples or scanning transmission electron microscopy (STEM), where EELS image formation depends on the interference of different Fourier components of the incident electron wave function.

In this paper EELS image localization and formation is examined, with particular reference to STEM imaging. Recent advances in aberration correction have allowed resolution in the STEM of less than 1 Å in the case of annular dark field (ADF) imaging (Nellist et al., 2004). The next generation of aberration corrected machines promises resolution of near 0.5 Å (TEAM Project, 2000). The localization of the EELS interaction for STEM has been examined by considering the width of single atom images (Kohl and Rose, 1984; Cosgriff et al., 2005). The core-loss EELS image width is a complicated function of binding energy, probe size and detector geometry.

These results however ignore the channelling of the incident electrons within the sample. In this paper the process of STEM image formation based on core-loss EELS is examined using an optical potential formulation, with absorption due to thermal diffuse scattering (TDS) included as an imaginary term in the potential. The presence of heavy columns with the crystalline sample leads to large angle scattering of the incident electron beyond the EELS detector, as well as an attenuation of the elastic intensity. The 'focussing' of the electron probe by the atomic columns is also considered.

2. Theory

A general expression for the inelastic cross section of fast electrons incident on a sample of thickness t and cross-sectional area A may be written as (Allen and Josefsson, 1995; Allen et al., 2006)

$$\sigma(\vec{\Gamma}) = \frac{2\pi m}{h^2 k}\int_0^t \int_A \int_A \psi_0^*(\vec{\Gamma}, \vec{r}_\perp, z) W(\vec{r}_\perp, \vec{r}'_\perp) \times \psi_0(\vec{\Gamma}, \vec{r}'_\perp, z)\, \mathrm{d}\vec{r}_\perp\, \mathrm{d}\vec{r}'_\perp\, \mathrm{d}z. \quad (1)$$

The vector $\vec{\Gamma}$ serves as a place holder for the relevant variables for a given experimental procedure. For example, for plane-wave illumination, where the incident beam is tilted with respect to the sample it describes the incident electrons wave

* Corresponding author.
E-mail address: oxleymp@ornl.gov (M.P. Oxley).

0968-4328/$ – see front matter. Published by Elsevier B.V.
doi:10.1016/j.micron.2007.10.020

vector $\vec{k}$. For the case of STEM it describes probe position $\vec{R}$. In Eq. (1), m is the relativistic electron mass, h is Planck's constant, $k = |\vec{k}|$ and $\psi_0(\vec{\Gamma}, \vec{r}_\perp, z)$ describes the elastic wave function of the incident electron within the sample.

The term $W(\vec{r}_\perp, \vec{r}'_\perp)$ is an effective nonlocal potential, in the projected potential approximation, and describes the inelastic scattering process of interest, for example EELS and energy dispersive X-ray analysis (EDX). It may be written in the form (Oxley et al., 2005),

$$W(\vec{r}_\perp, \vec{r}'_\perp) = \frac{h^2 k}{2\pi m A t} \sum_{\vec{h},\vec{g}} \mu_{\vec{h},\vec{g}} \exp(2\pi i \vec{h} \cdot \vec{r}_\perp) \times \exp(-2\pi i \vec{g} \cdot \vec{r}'_\perp), \quad (2)$$

where $\vec{h}$ and $\vec{g}$ are variables in the Fourier transform space. For inner-shell ionization from atom type β the inelastic scattering coefficients $\mu_{\vec{h},\vec{g}}$ are calculated using (Allen and Josefsson, 1995)

$$\mu_{\vec{h},\vec{g}} = \frac{1}{2\pi k V_c} \sum_j \exp[-M_{\beta_j}(\vec{g} - \vec{h})] \times \exp[2\pi i(\vec{g} - \vec{h}) \cdot \vec{\tau}_{\beta_j}] f(\vec{h}, \vec{g}). \quad (3)$$

The sum over j includes all atoms of type β within the unit cell of volume V_c. The Debye–Waller factor $M_\beta(\vec{g} - \vec{h})$ accounts for the thermal motion of the target atoms. The atomic scattering form factor $f(\vec{h}, \vec{g})$ is given by

$$f(\vec{h}, \vec{g}) = \frac{1}{2\pi^3 a_0^2} \int \int K' \frac{\sum_{i,f} F^*_{i,f}(\vec{Q}_{\vec{h}}, E_f) F_{i,f}(\vec{Q}_{\vec{g}}, E_f)}{|\vec{Q}_{\vec{h}}|^2 |\vec{Q}_{\vec{g}}|^2} \, dE_f \, d\Omega_{K'}, \quad (4)$$

where a_0 is the relativistically corrected Bohr radius. The momentum transfer to the crystal is $h\vec{Q} = h(\vec{K} - \vec{K}')$ where $\vec{K}$ and $\vec{K}'$ are the refraction corrected wave vectors of the incident and scattered electron, respectively. The vector $\vec{Q}_{\vec{h}}$ is defined as $\vec{Q}_{\vec{h}} = \vec{Q} + \vec{h}$. The indices i and f define the initial and final states of the target electron, and E_f is the energy of the ejected electron. For EELS the detector geometry is defined by the integration over $d\Omega_{K'}$ and dE_f defines the energy window over which the EELS signal is integrated. For EDX these integrations cover all possible scattering angles and energy losses.

The transition matrix element from the initial state to final state is given by

$$F_{i,f}(\vec{Q}_{\vec{g}}, E_f) = \int u^*_f(E_f, \vec{r}) \exp[2\pi i(\vec{Q}_{\vec{g}} \cdot \vec{r})] u_i(\vec{r}) \, d\vec{r} \equiv \langle f | \exp[2\pi i(\vec{Q}_{\vec{g}} \cdot \vec{r})] | i \rangle, \quad (5)$$

where $u_i(\vec{r})$ defines the initial state and $u_f(E_f, \vec{r})$ the final state of the target electron, respectively.

We describe $W(\vec{r}_\perp, \vec{r}'_\perp)$ as an effective nonlocal potential because it is a function of two independent real-space vectors and its Fourier components $\mu_{\vec{h},\vec{g}}$ are similarly a function of two independent reciprocal space vectors. Examination of Eq. (1) shows that the cross section is a function of the product of the incident wave function expressed in terms of two different real space coordinates. It is hence not a function of the intensity of the incident wave function alone. It may in this sense be considered a "coherent" cross section, dependant not only on the amplitude, but also the phase of the incident electron wave function as it propagates through the specimen. The expressions given here are a generalization of the expressions of Yoshioka, which in turn are a generalization of the Bethe scattering equations (Allen and Josefsson, 1995; Yoshioka, 1957; Bethe, 1928). Similar expressions have been derived, using different starting points, independently by other authors (Dudarev et al., 1993; Dywer, 2005). The sum over the product of transition matrix elements seen in Eq. (4) is closely related to the mixed dynamical form factor of Rose (1976). The effective nonlocality is implicit in all these formulations.

The cross-section expression in Eq. (1) can be rewritten in reciprocal space form as (Allen et al., 2003),

$$\sigma(\vec{\Gamma}) = \int_t \sum_{\vec{h},\vec{g}} \Psi^*_h(\vec{\Gamma}, z) \Psi_g(\vec{\Gamma}, z) \mu_{\vec{h},\vec{g}} \, dz. \quad (6)$$

It is useful to consider some special forms of Eq. (6).

2.1. Plane-wave illumination

First let us consider the case where we have plane-wave illumination (wave vector $\vec{k}$) and channelling of the incident electron is not significant. Eq. (6) can then be reduced to the form,

$$\sigma(k) = t|\Psi_0(k)|^2 \mu_{\vec{0},\vec{0}}, \quad (7)$$

which (ignoring some normalization factors) produces results similar to Egerton's programs SIGMAK and SIGMAL (Egerton, 1979, 1981). In previous work this has also been referred to as the kinematic cross section (Allen and Josefsson, 1995). The cross section is a function of only the magnitude of the incident wave vector $k = |\vec{k}|$.

For crystalline samples, diffraction leads to significant contributions to the cross section from Fourier components of the incident electron wave function other than $\Psi_0(\vec{k})$. In this case we rewrite Eq. (6) in the form

$$\sigma(\vec{k}) = \int_t \sum_{\vec{h},\vec{g}} \Psi^*_h(\vec{K}, z) \Psi_g(\vec{K}, z) \mu_{\vec{h},\vec{g}} \, dz. \quad (8)$$

The Fourier components of the incident electron wave function now become functions of the beam/crystal orientation and the refracted wave vector $\vec{K}$ as well as the depth within the crystal z. For EDX the variation with X-ray yield as a function of beam orientation has been used to develop the method of atom location by channelling enhanced microanalysis (ALCHEMI), see for example Spence and Taftø (1983); Andserson (1997); Oxley et al. (1999a) and references contained within. An example of an EDX cross section as a function of beam orientation, and simulation based on Eq. (8) is shown in Fig. 1.

Similar cross-section variation, as a function of beam orientation, is also observed for EELS, as shown in Fig. 2.

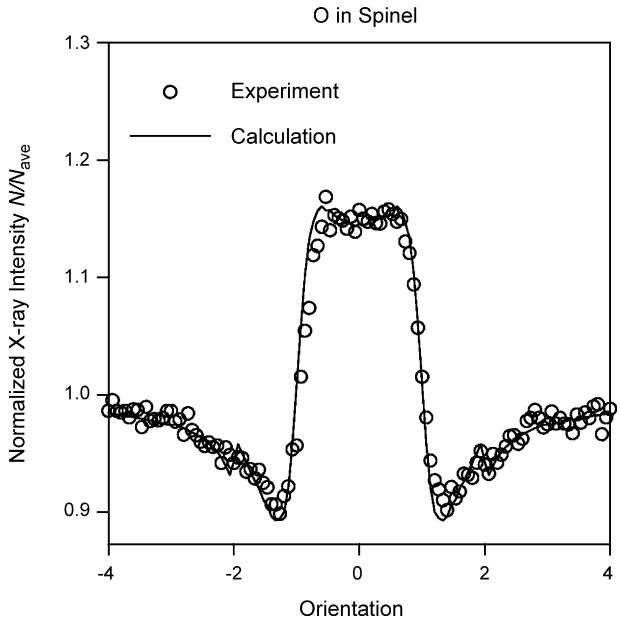

Fig. 1. Normalized EDX cross section, N/N_{ave}, for the oxygen K-shell for 120 keV electrons incident on spinel for $\langle 4\,0\,0\rangle$ systematic row conditions. A value of one on the orientation axis means that $\langle 4\,0\,0\rangle$ is in the exact Bragg orientation. This figure is reproduced from Oxley and Allen (2003).

There are two significant differences between the simulation of EDX and EELS cross sections. For small detector semi-angles (such as the 0.15 mrad collector used in Fig. 2) it is essential to account for the channelling of the scattered electrons, which is not included in the expressions above. Simulations for Fig. 2 have hence been carried out using a double channeling Bloch wave formulation (Josefsson and Allen, 1996). In addition, a full nonlocal description as described above is essential for most EELS simulations. In Fig. 2(b) a common local approximation $[f(\vec{h},\vec{g}) \approx f(\vec{h}-\vec{g},\vec{0})]$ is compared with a full nonlocal description and experiment. The local approximation fails to reproduce the peaks observed about the first and second Bragg angles. Local approximations, and their validity, will be discussed in more detail below.

2.2. STEM imaging

For inelastic STEM imaging Eq. (6) is rewritten in terms of probe position $\vec{R}$

$$\sigma(\vec{R}) = \int_t \sum_{\vec{h},\vec{g}} \Psi_h^*(\vec{R},z)\Psi_g(\vec{R},z)\mu_{\vec{h},\vec{g}}\,\mathrm{d}z. \tag{9}$$

Unlike the plane wave case, the wave function of the STEM probe itself contains Fourier components other than ψ_0 and the vectors $\vec{h}$ and $\vec{g}$ are related to the reciprocal space vectors calculated using a suitable super-cell rather than the crystallographic unit cell (Allen et al., 2003). For smaller detectors, the channelling of the inelastically scattered electron (which is ignored in this formulation) may also become significant. This is the subject of ongoing work and is beyond the scope of this paper.

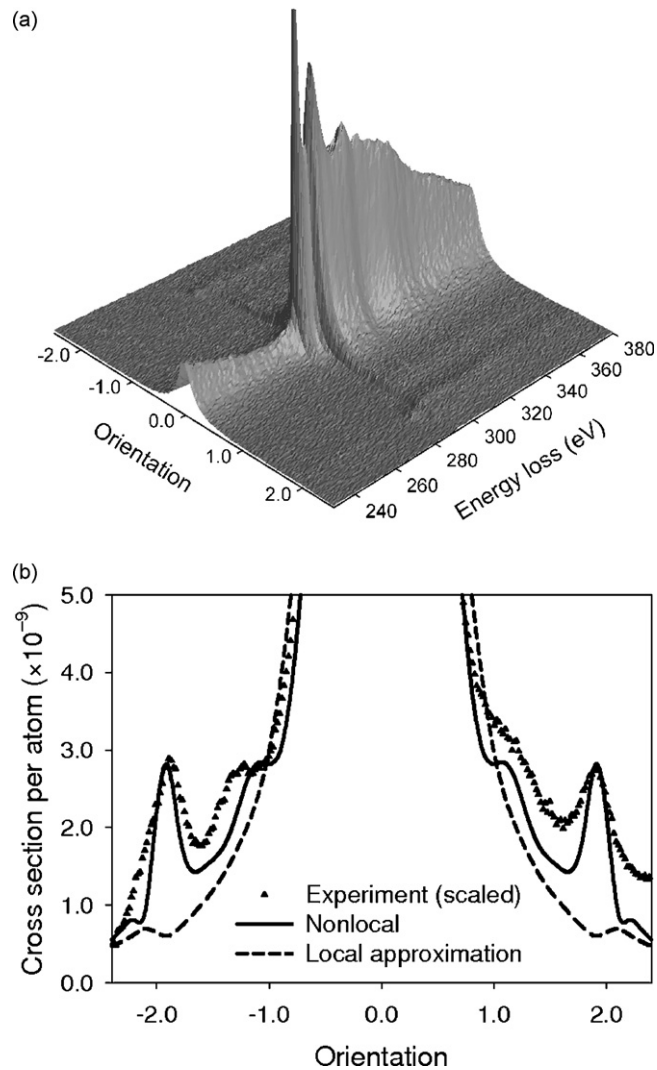

Fig. 2. (a) Extract from the energy loss spectrum taken from graphite as a function of tilt along the $[1\,0\,\bar{1}\,0]$ systematic row. (b) Comparison of experimental and simulated data, focussing on the Bragg peaks. The incident energy was 200 keV and a detector semi-angle of 0.15 mrad was used. This figure is reproduced from Allen et al. (2006).

In order to examine the details of the effective EELS interaction, it is common to consider the image that would be formed from an isolated atom. Ignoring the thermal motion of the atom, and assuming a nominal 'thickness' of 1 Å, we can rewrite Eq. (9) as

$$\sigma(\vec{R}) = \frac{1}{2\pi k V_{\mathrm{c}}} \sum_{\vec{h},\vec{g}} \Psi_h^*(\vec{R},0)\Psi_g(\vec{R},0)\, f(\vec{h},\vec{g}). \tag{10}$$

In the absence of diffraction, the range of the sum over $\vec{h}$ and $\vec{g}$ is restricted to those reciprocal space vectors within the probe forming aperture.

3. Results and discussion

The formation of STEM images based on core-loss EELS is complicated by many factors. The localization of the STEM EELS image depends on the size of the incident probe, but also

on the nonlocal nature of the effective ionization potential. As probes become smaller, this nonlocality makes the interpretation of images more difficult, with prominent volcanoes occurring above the atomic site when the probe forming aperture is larger than the detector. The localization of single atom images, based on O K-shell ionization, is a function of both probe and detector size. For smaller detector sizes, the localization of the image is limited by the probe forming aperture. For larger detectors increasing the probe forming aperture beyond 30 mrad results in little additional localization, suggesting the the limit on the localization is imposed by the ionization potential. It should be noted that the localization of STEM EELS images will depend also on the incident energy and the atom/orbital from which the ionization occurs, and these results represent a rule of thumb only.

The validity of two possible local approximations has been shown to have limited ranges of applicability. Their validity

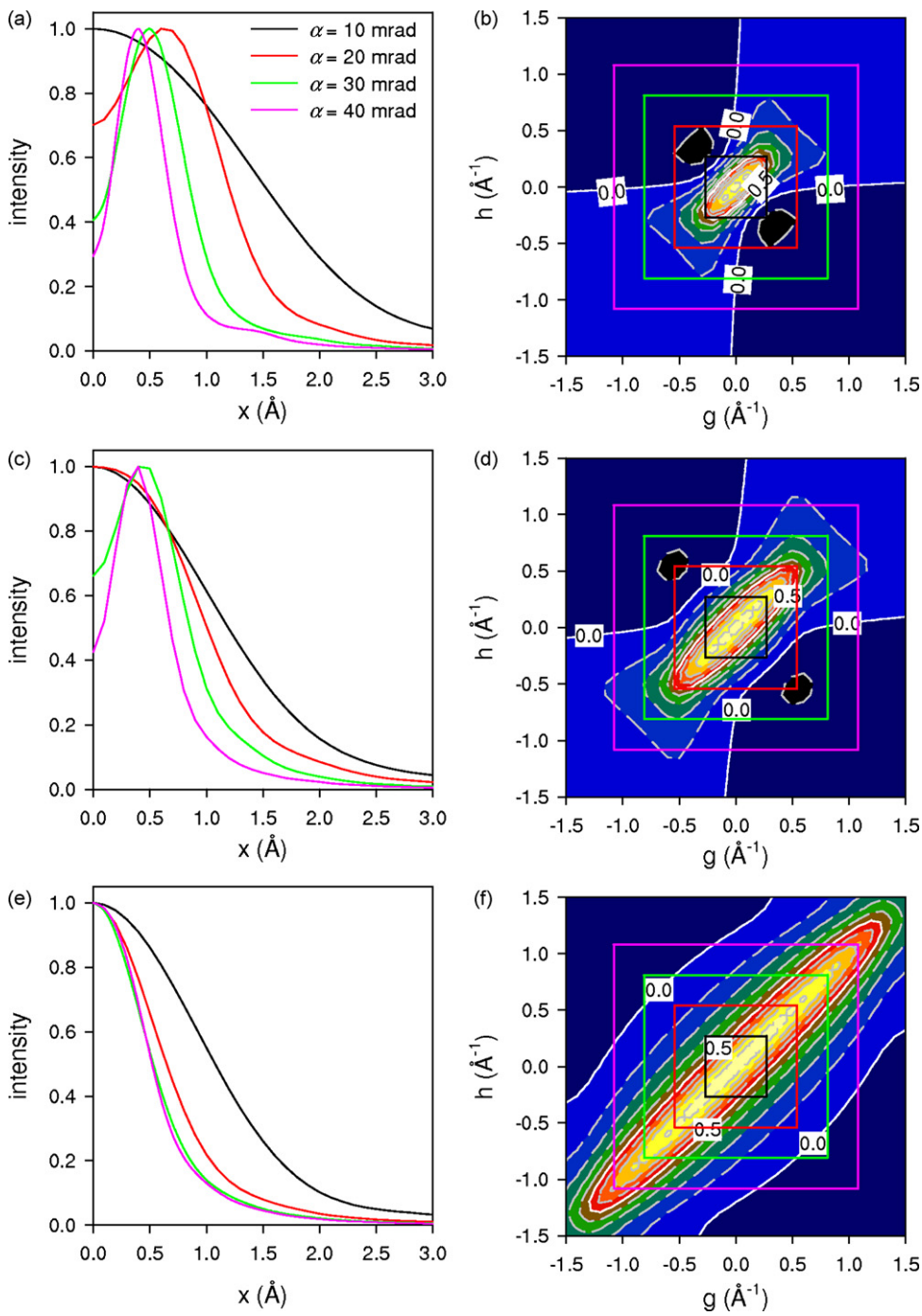

Fig. 3. Single atom STEM EELS images, based on O K-shell ionization, as a function of probe forming aperture α and related atomic scattering form factors for detector semi-angles of $\beta = 10$ mrad (a and b), $\beta = 20$ mrad (c and d) and $\beta = 50$ mrad (e and f). All probes have 100 keV incident energy and are aberration free. The cutoffs imposed by the probe forming apertures are indicated by the squares.

also needs to be examined on a case by case basis and a full nonlocal calculation is preferred.

The interpretation of STEM EELS images is further complicated by the channelling of the electron probe through the sample. There are significant differences in the way probes of different probe forming apertures propagate through the crystal. Channeling is also strongly dependant on the effective atomic weight of atomic columns, which depends on the atomic species present and the lattice spacing of the crystal. Heavier columns result in a strong focusing of the probe. This however results in more high angle scattering, both elastic and due to TDS, beyond the EELS detector. These complications point to the need for simulation as an aid to experimental interpretation.

3.1. Single atom imaging: STEM EELS image localization

The effective ionization potential $W(\vec{r},\vec{r}')$ and the atomic scattering form factors $f(\vec{h},\vec{g})$ are functions of detector semi-angle, incident energy and the threshold energy of the ionization event. In Fig. 3 we compare single atom STEM EELS images based on O K-shell ionization, for 100 keV incident electrons and a range of probe forming apertures and detector semi-angles. All probes are assumed to be aberration free and the calculated EELS signal is integrated over an energy window of 40 eV above threshold. Atomic scattering form factors for parallel reciprocal space lattice vectors are also shown. For ease of comparison, images and form factors are normalized to a maximum of one.

In Fig. 3(a) the single atom images are formed using a detector collection semi-angle of $\beta = 10$ mrad and probe forming apertures of $\alpha = 10-40$ mrad. As the probe forming aperture is increased, the image becomes more localized about the atomic site. With the exception of the smallest probe forming aperture, $\alpha = 10$ mrad, there is a reduction in intensity, or 'volcano', above the atomic site. This may be understood by examining the atomic form factors in Fig. 3(b), where a subset of form factors for parallel reciprocal lattice vectors are shown. The form factors are strongly peaked about the origin ($\vec{h} = \vec{g} = \vec{0}$) and reduce rapidly along the diagonal. There are significant areas on the anti-diagonal where the form factors becomes negative, and the contribution to the EELS image from these form factors is itself negative above the atomic site. As the probe forming aperture is increased in size (indicated by the squares on the form factor plot), more negative values are included and the volcano becomes more pronounced. Fig. 3(c) and (d) shows images and form factors respectively for a detector semi-angle $\beta = 20$ mrad. Volcanos occur only for probe forming apertures $\alpha = 30$ mrad and above. Examination of the form factors in this case shows that the peak about the origin has extended along the diagonal, when compared to the case where $\beta = 10$ mrad. This leads to a greater positive contribution to the image as α is increased. The strongly negative values of the form factors have also occur further away from the diagonal. This effect is seen more clearly for the case of $\beta = 50$ mrad. The images in Fig. 3(e) have no volcanoes. The spreading of the form factor intensity along the diagonal, seen in Fig. 3(f), means that there is a significant positive contribution to the images for all probe forming apertures. Only the largest aperture has any significant overlap in the region of negative form factors.

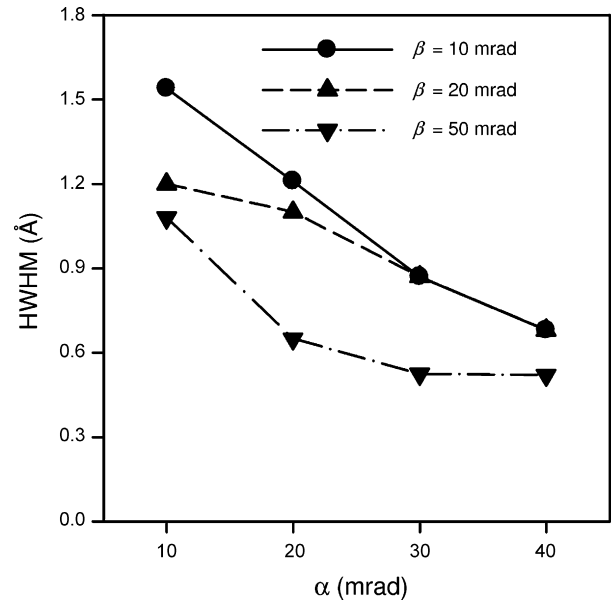

Fig. 4. Half width at half maximum (HWHM) of single atom STEM EELS images, based on O K-shell ionization, as a function of probe forming aperture α and detector semi-angle β.

It is interesting to compare the image localization of the O K-shell STEM EELS images as a function of probe forming aperture and detector size. The half width at half maximum (HWHM) of the images is plotted in Fig. 4 for the images discussed above. For $\beta = 10$ mrad, there is an almost linear reduction in the HWHM of the image for increasing probe forming aperture size. This suggests that the limiting factor in image localization in this case is due to the probe size rather than the nature of the inelastic interaction. When the detector semi angle is increased to $\beta = 20$ mrad, there is initially a significant reduction of the HWHM for small α when compared to the $\beta = 10$ mrad case. However, for larger probe forming apertures, the HWHMs of the 10 and 20 mrad images are indistinguishable. There is again a general reduction in image localization as the probe size is reduced. For the larger $\beta = 50$ mrad detector, the image localization initially reduces with increasing α, but there is no significant reduction in image width for $\alpha > 30$ mrad. This suggests that the image localization is limited by the interaction in this case. It needs to be noted that the image localization is a function of the orbital which is ionized and also the incident energy, and these trends need to be examined on a case by case basis.

3.2. The local approximation

Because the the effective scattering potential $W(\vec{r},\vec{r}')$ is a function of two real space variables it is difficult to visualize. In order to aid interpretation a so called 'local' approximation is often made, which allows the construction of a potential that is a function of a single real space coordinate. Two common local approximations are $f(\vec{h},\vec{g}) \approx f(\vec{h}-\vec{g},\vec{0})$ and

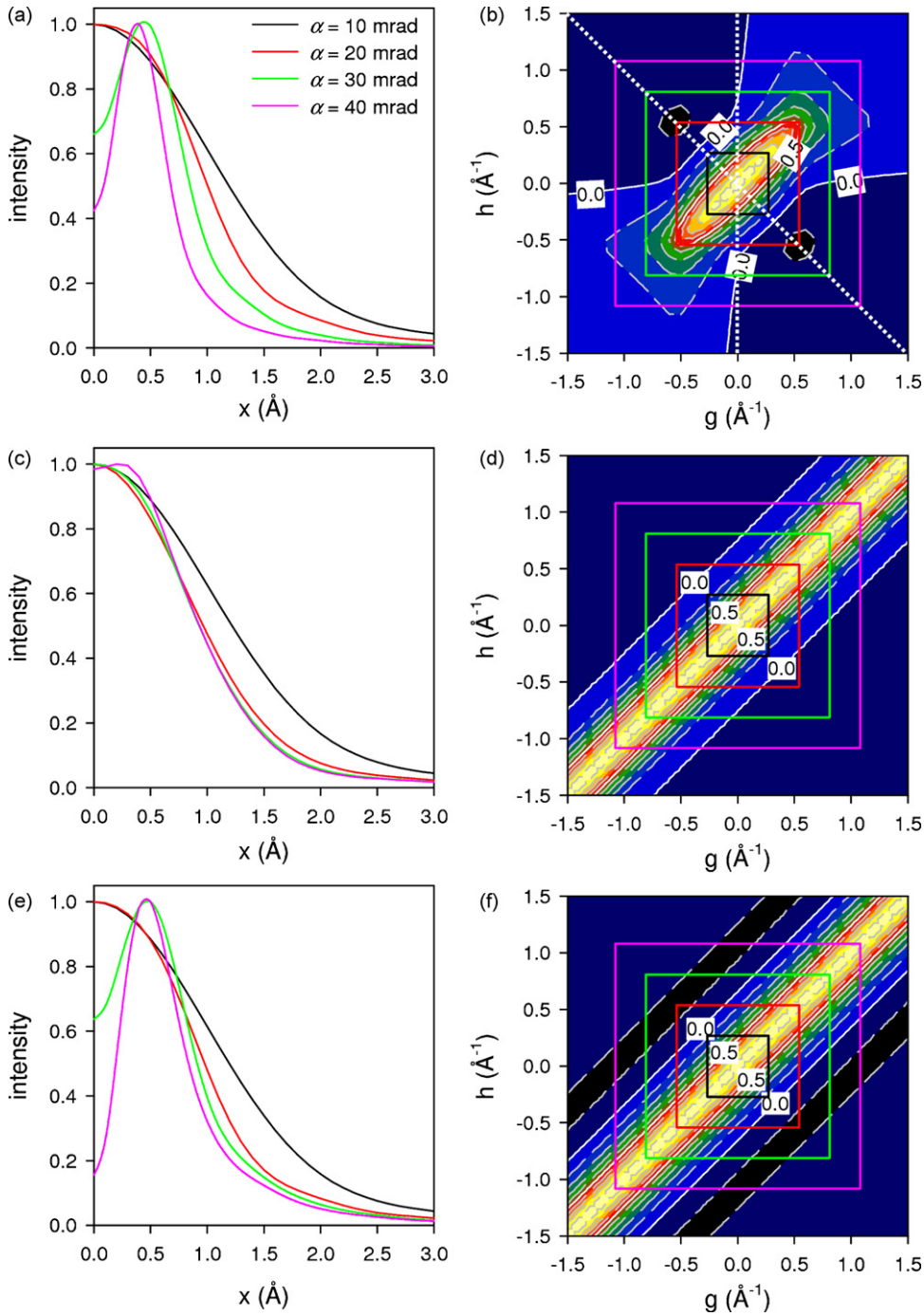

Fig. 5. Single atom STEM EELS images, based on O K-shell ionization, as a function of probe forming aperture α and related atomic scattering form factors for detector semi-angle of $\beta = 20$ mrad. Nonlocal calculation (a and b), and local approximations $f(\vec{h},\vec{g}) \approx f(\vec{h}-\vec{g},\vec{0})$ (c and d) and $f(\vec{h},\vec{g}) \approx f[-(\vec{h}-\vec{g})/2,(\vec{h}-\vec{g})/2]$ (e and f). All probes have 100 keV incident energy and are aberration free. The cutoffs imposed by the probe forming apertures are indicated by the squares.

$f(\vec{h},\vec{g}) \approx f[-(\vec{h}-\vec{g})/2,(\vec{h}-\vec{g})/2]$. In Fig. 5 (a) and (b), the nonlocal results for $\beta = 20$ mrad are reproduced for ease of comparison with these two approximations.

The first local approximation includes only the form factors along the vertical dotted line through $g = 0$ shown on Fig. 5(b). The resulting images and form factors are shown in Fig. 5(c) and (d), respectively. Because the most negative form factors are excluded, only the largest probe forming aperture produces a volcano. In addition there is no significant reduction in the image localization for $\alpha \geq 20$ mrad. The second local approximation includes only form factors on the anti-diagonal of Fig. 5(b). This in general overestimates the contribution of the negative form factors. While the images shown in Fig. 5(e) seem in good agreement with the nonlocal calculations in Fig. 5(a), for the largest probe forming aperture, $\alpha = 40$ mrad, the depth of the volcano over the atomic site is overestimated. Calculations have shown that, for some combinations of detector and probe forming apertures, the intensity can in fact

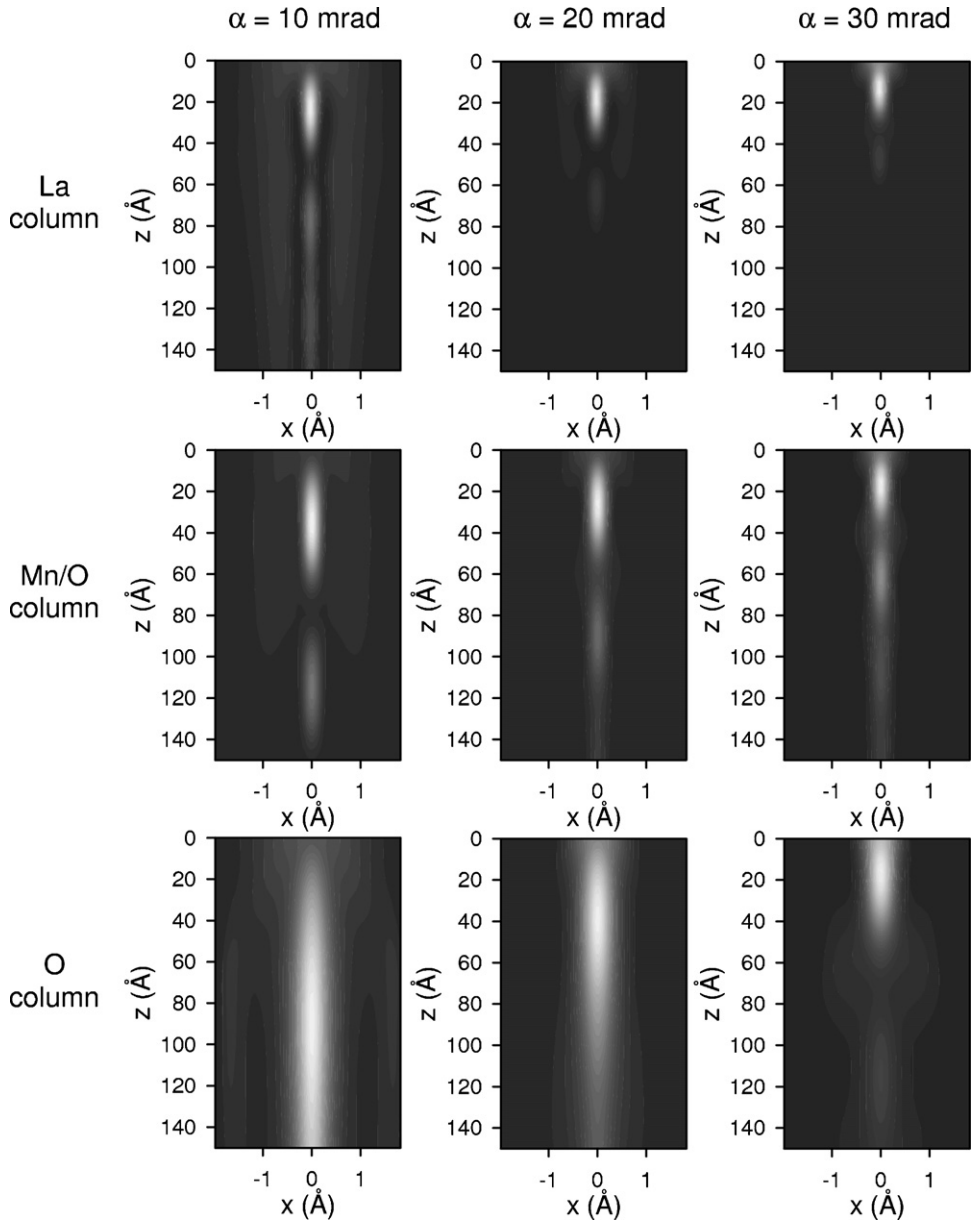

Fig. 6. Incident electron intensity as a function of depth within a $LaMnO_3$crystal in the [0 0 1] zone axis orientation.

be negative above the atomic site which is clearly unphysical. Both these approximations have a limited range of applicability and a full nonlocal approximation is preferred.

If the interaction is indeed local, the two local approximations can be easily shown to be equivalent, and as a general rule, if the probe-forming aperture is smaller than the detector semi-angle, a local approximation is reasonable. It is worth considering the atomic form factors for $\beta = 50$ mrad shown in Fig. 3(f). It is clear that, for the probe-forming apertures considered here, that both local approximations would provide an excellent description of the atomic form factors.

3.3. Channelling of the electron probe

As shown Figs. 1 and 2, the channelling of the incident electron plays a crucial role in determining the resulting core-loss EELS intensity. In Fig. 6 the intensity of 100 keV electron STEM probes is plotted as a function of depth within a $LaMnO_3$ crystal in the [0 0 1] zone axis orientation for probe forming apertures of $\alpha = 10 - 30$ mrad. Probes are positioned above the La, Mn/O and O columns. The channelling of the electron probe is strongly dependent on both the probe forming aperture and the effective atomic weight of the column. As a general rule, as the probe forming aperture is increased, the peak in electron intensity on the column moves toward the entrance surface of the crystal, where the aberration free probes are focused. For the heaviest (La) column, only a probe forming aperture of $\alpha = 10$ mrad provides any significant intensity at depths of more than 60 Å. For $\alpha = 30$ mrad, only the first 30 Å of the La column is strongly illuminated. Focussing the probe further into the crystal will result in more of the column being illuminated and form the basis of depth sectioning based on EELS (D′Alfonso et al., 2007).

It is useful to compare the channelling on the Mn/O and O columns. Both columns contain the same number of O atoms and, excluding channelling effects, the same O K-shell signal might be expected. The intensity on the Mn/O columns is peaked near the entrance surface, more so for the finer probes. Clearly most of the O K-shell signal will be derived from the first 40–60 Å of the crystal. For the lighter O columns, the larger probes illuminate most of the column. Only for the $\alpha = 30$ mrad probe is the intensity peaked about the entrance surface. This may be understood by considering the reduced depth of field of the electron probe as the probe forming aperture is increased. The light O columns do not have as strong a 'focussing' effect as the heavier columns, except perhaps at the entrance surface where the transition of the probe from vacuum to O column is most pronounced. It is only for the smallest probe that similar regions of the Mn/O and O columns are strongly illuminated. However, it should be noted that in all cases the Mn/O and O columns are illuminated by 20% or more of the maximum column intensity for most depths within the crystal. The La column has minimal illumination beyond a depth of 60 Å for other than the $\alpha = 10$ mrad probe.

The formation of STEM EELS images is not simply a function of probe intensity, the dependence of the image on the phase of the incident electron wave function is seen explicitly in Eq. (1). In addition, while examination of the probe intensity for probes placed above atomic columns may provide some insight into the origin of the STEM EELS signal, probes positioned near atomic columns are attracted toward the columns further complicating the image formation process. The absorption of electrons from the elastic wavefunction due to TDS leads to high angle scattering beyond the EELS detector, resulting in a reduction in signal above heavier atomic columns as sample thickness increases.

STEM EELS images based on O K-shell ionization in $LaMnO_3$are shown as a function of specimen thickness and probe size in Fig. 7. A detector semi-angle of $\beta = 20$ mrad is used in all cases. The top row shows images formed for a 'crystal' with a nominal thickness $t = 1$ Å. This is essentially just the overlap of single atom images (as shown in Fig. 3(c). The central Mn/O column is surrounded by four O columns at a distance of less than 2 Å. Each O column has only two neighboring Mn/O columns. For $\alpha = 10$ mrad, the single atom image is broad and there is strong overlap between the different sites. This results in a maximum signal on the Mn/O column. The width of the single atom image means there is significant signal when the probe is located above the La column at the

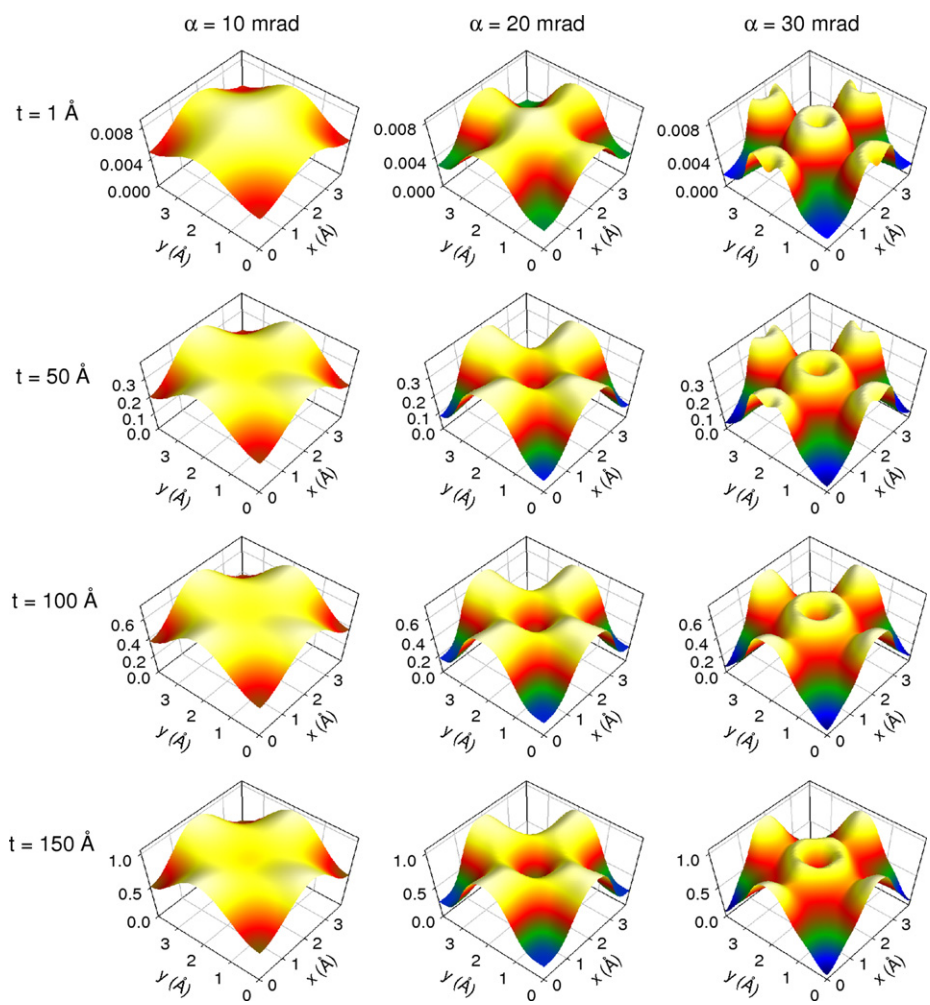

Fig. 7. O K-shell STEM EELS image intensity as a function of specimen thickness and probe forming aperture for a $LaMnO_3$crystal in the [0 0 1] zone axis orientation. A detector semi-angle of $\beta = 20$ mrad is used in all cases.

corners of the unit cell. As the probe forming aperture is increased, the signals become more localized about the atomic sites. This at first leads to a reduction of the signal above the La columns, and eventually for $\alpha = 30$ mrad, individual volcanoes are seen above the columns containing O.

As the specimen thickness increases, there is in general a decrease in the relative intensity above the Mn/O column compared to that above the O column. For $\alpha = 10, 20$ mrad this results in the maximum intensity being above the O columns. In both cases there is little qualitative change in the image beyond $t = 50$ Å. For $\alpha = 30$ mrad the evolution of the image with increasing thickness is somewhat more complicated. For a thickness of 50 Å the volcanoes above the O columns are still evident, while the volcano above the Mn/O column has become more pronounced due to TDS absorption. While the volcano above the Mn/O column remains, the intensity above the O columns gradually flattens out and the image is peaked above the columns when $t = 150$ Å. A possible explanation for this phenomena is the broadening of the probe in real space for greater specimen thickness, leading to contributions to the image that are peaked above the column, as seen in Fig. 3(c).

4. Conclusions

STEM image formation based on core-loss EELS is influenced by many factors. Aberration correction allows the formation of smaller probes, and potentially more localized STEM EELS images. For the case of ionization from the O K-shell examined here it is seen, that for smaller detectors, there is a reduction in image width as the probe size decreases. This suggests that the probe size rather than the ionization interaction is the limiting factor for image localization. For larger detectors considered here, the image is in general more localized, however there is no appreciable reduction in image localization for the probes with probe-forming apertures $\alpha \geq 30$ mrad. This suggests, that in this case, image localization is limited by the nature of the interaction itself.

Another important factor in determining the shape and intensity of the EELS image is the channelling of the incident electron by the sample. This may lead to unexpected results. For example, in the case of O K-shell ionization in $LaMnO_3$, there is a significant reduction in signal strength above the Mn/O column when compared to that above the O column, a result that might naively be interpreted as a variation in O concentration. Simulation thus forms an essential adjunct to experiment as an aid to interpretation.

Acknowledgments

This research was sponsored by the Office of Basic Energy Sciences, Division of Materials Sciences and Engineering, U.S. Department of Energy and by appointment (MPO) to the ORNL Postdoctoral Research Program administered jointly by ORNL and ORISE and by the ORNL Laboratory Directed Research and Development Program.

References

Allen, L.J., Josefsson, T.W., 1995. Inelastic scattering of fast electrons by crystals. Phys. Rev. B 52, 3184–3198.

Allen, L.J., Findlay, S.D., Oxley, M.P., Rossouw, C.J., 2003. Lattice-resolution contrast from a focused coherent electron probe. Part I. Ultramicroscopy 96, 47–63.

Allen, L.J., Findlay, S.D., Oxley, M.P., Witte, C., Zaluzec, N.J., 2006. Modelling high-resolution electron microscopy based on core-loss spectroscopy. Ultramicroscopy 106, 1001–1011.

Andserson, I.M., 1997. ALCHEMI study of site distributions of 3d-transition metals in B2-ordered iron aluminides. Acta Mater. 45, 3897–3909.

Bethe, H., 1928. Theorie der Beugung von Elektronen an Kristallen. Ann. Phys. 17, 55–129.

Cosgriff, E.C., Oxley, M.P., Allen, M.P., Pennycook, S.J., 2005. The spatial resolution of imaging using core-loss spectroscopy in the scanning transmission electron microscope. Ultramicroscopy 102, 317–326.

D′Alfonso, A.J., Findlay, S.D., Oxley, M.P., Pennycook, S.J., van Benthem, K., Allen, L.J., 2007. Depth sectioning in scanning transmission electron microscopy based on core-loss spectroscopy. Ultramicroscopy 108, 17–28.

Dudarev, S.L., Peng, L.-M., Whelan, M.J., 1993. Correlations in space and time and dynamical diffraction of high energy electrons by crystals. Phys. Rev. B 48, 13408–13429.

Dywer, C., 2005. Multislice theory of fast electron scattering incorporating atomic inner-shell ionization. Ultramicroscopy 104, 141–151.

Egerton, R.F., 1979. K-shell ionization cross-sections for use in microanalysis. Ultramicroscopy 4, 169–179.

Egerton, R.F., 1981. SIGMAL: a program for calculating L-shell ionization cross sections. In: Bailey, G.W. (Ed.), Proceedings of the 39th Ann. Proc. Electron Micros. Soc. Am. Claitor's Publishing, Baton Rouge, Louisiana, pp. 198–199.

Egerton, R.F., 1996. Electron Energy-Loss Spectroscopy in the Electron Microscope. Plenum Press, New York.

Josefsson, T.W., Allen, L.J., 1996. Diffraction and absorption of inelastically scattered electrons for K-shell ionization. Phys. Rev. B 53, 2277–2285.

Kohl, H., Rose, H., 1984. Theory of image formation by inelastically scattered electrons in the electron microscope. Adv. Imaging Electron Phys. 65, 173–227.

Nellist, P.D., Chisholm, M.F., Dellby, N., Krivanek, O.L., Murfitt, M.F., Szilagyi, Z.S., Lupini, A.R., Borisevich, A., Sides, W.H., Pennycook, S.J., 2004. Direct sub-Angstrom imaging of a crystal lattice. Science 305, 1741.

Oxley, M.P., Allen, L.J., Rossouw, C.J., 1999a. Correction terms and approximations for atom location by channelling enhanced microanalysis. Ultramicroscopy 80, 109–124.

Oxley, M.P., Allen. L.J., 2003. ICSC: a program for calculating inelastic scattering cross sections for fast electrons incident on crystals. J. Appl. Cryst. 36, 940–943.

Oxley, M.P., Cosgriff, E.C., Allen, L.J., 2005. Nonlocality in imaging. Phys. Rev. Lett. 94, 203906.

Rose, H., 1976. Image formation by inelastically scattered electrons in electron microscopy. Optik 45, 139–158.

Spence, J.C.H., Taftø, J., 1983. ALCHEMI- a new technique for locating atoms in small crystals. J. Microsc. 130, 147–154.

TEAM Project 2000, url: http://ncem.lbl.gov/team3.htm.

Yoshioka, H., 1957. The effect of inelastic waves on electron diffraction. J. Phys. Soc. Jpn. 12, 618–628.